Combustion and Flame 238 (2022) 111880

Contents lists available at ScienceDirect

Combustion and Flame

journal homepage: www.elsevier.com/locate/combustflame

A numerical study on the combustion of a resolved carbon particle

Ewa Karchniwy[a,b,*,*], Nils Erland L. Haugen[c], Adam Klimanek[a]

[a] Department of Thermal Technology, Silesian University of Technology, Konarskiego 22, Gliwice 44-100, Poland
[b] Department of Energy and Process Engineering, Norwegian University of Science and Technology, Kolbjørn Hejes vei 1B, Trondheim NO-7491, Norway
[c] SINTEF Energi A.S., Sem Saelands vei 11, Trondheim 7034, Norway

ARTICLE INFO

Article history:
Received 16 August 2021
Revised 13 November 2021
Accepted 15 November 2021

Keywords:
Resolved particle
Char conversion
Overset grid
Mutliphase reactive flows
Solid fuel combustion

ABSTRACT

Combustion of a single, resolved carbon particle is studied using a novel numerical approach that makes use of an overset grid. The model is implemented into the framework of a compressible Direct Numerical Simulation (DNS) code. A method to artificially reduce the speed of sound is presented. For Mach numbers lower than ~0.1 this method may dramatically improve numerical efficiency without affecting any physical aspects except for the acoustics. The ability of the model to simulate solid fuel combustion is demonstrated and all parts of the model are validated against experimental and numerical data. A sensitivity of the carbon conversion rate to selected parameters (diffusion coefficients and homogeneous and heterogeneous kinetics) is investigated. A strong dependence on the oxygen diffusivity is observed and explained.

1. Introduction

Solid fuels are among the most important energy sources worldwide. On one hand, some countries, like e.g. China, India or Poland, are still vastly dependent on coal [1]. On the other hand, the contribution to the energy production from solid fuels in the form of biomass and refuse-derived fuel is increasing every year [2]. Due to its strong effect on global warming, emission of carbon dioxide from solid fuels conversion is a serious environmental problem. This, in connection with the global increase in energy demand [3], necessitates development of low-emission and efficient solid fuel-based technologies. Such technologies cannot be designed without a thorough knowledge about fuel properties and understanding of the underlying fuel conversion phenomena. This understanding is currently provided by experiments and by numerical simulations. Experimental investigation of solid fuels combustion is difficult because of complex physical and chemical processes occurring at different scales. As a consequence, information provided by experiments may not be complete. A deeper insight can be gained through detailed numerical simulations, in which all flow scales are resolved on a numerical grid. It should be stressed, however, that both research methods are complementary and equally important.

In Direct Numerical Simulation (DNS) studies on solid fuels conversion in turbulent systems, particles are commonly represented as point sources. This approach has previously been employed to study different aspects of pulverized coal combustion, for example in jet flames [4–6] and mixing layers [7–9]. The approximation of point particles is applicable only to very small particles, i.e. to particles with diameters smaller than Kolmogorov length scales of turbulence [10]. Also, in such simulations, interactions between the fluid and particles must be modeled using closure expressions. These expressions can be supplied by simulations in which the particle surface and its boundary layer are resolved on the numerical mesh. Even though such resolved simulations are typically limited to one or a few particles, this approach has a great potential to provide an understanding of the solid fuel conversion and gas-particle interactions at a very fundamental level. The resolved particle approach has recently been employed in several numerical investigations of coal or carbon conversion. Devolatilization and ignition stages of the resolved pulverized coal particle were considered by Vascellari et al. [11], whose studies were extended by Tufano et al. [12] to account for different atmospheres and a more accurate description of the volatile yield and composition. The same research group further broadened the focus of their studies on resolved coal particles by considering particle arrays [13], higher particle Reynolds numbers and effects of turbulence [14]. A number of publications neglect the devolatilization and investigate resolved char particle combustion and gasification in steady state. For example, Kestel et al. [15] studied the impact of steam content and

* Corresponding author at: Department of Thermal Technology, Silesian University of Technology, Konarskiego 22, Gliwice 44-100, Poland.
E-mail address: ewa.karchniwy@sintef.no (E. Karchniwy).

https://doi.org/10.1016/j.combustflame.2021.111880

Reynolds number on the char oxidation in air, while the effects of the ambient gas temperature, gas velocity and oxygen mass fractions in O_2/CO_2 atmosphere were considered by Richter et al. [16]. A similar analysis was also performed by Safronov et al. [17] who indicated differences in combustion behavior between micro- and milimeter-sized particles. The conversion of a collection of resolved carbon particles was also investigated in a similar way by Schulze et al. [18]. Furthermore, the steady state approach was employed in a few studies [19–21] that attempted to resolve porous particle and understand intrinsic reactivity. It was shown that both porosity and pore structure can affect char conversion.

As demonstrated by the above-mentioned examples, a great deal of understanding can be reached with the steady state assumption. However, all transient phenomena and processes (ignition, volatiles burnout, progress of char conversion, combustion in non-laminar flow) require unsteady approach. The first transient simulations of resolved particle combustion in a non-quiescent (two-dimensional) flow were performed by Lee et al. [22] using the spectral element method. Recently, Farazi et al. [23] used an unsteady approach and a detailed chemical mechanism, and investigated char particle combustion in air and oxy-fuel atmospheres. The combustion characteristics in these two atmospheres were explored, as well as interactions between kinetics and mass transfer. This work was further extended to particle arrays by Sayadi et al. [24]. Another study on the resolved particle conversion in which the governing equations were solved in their unsteady form was done by Luo et al. [6]. In their work, an immersed boundary method and a simple semi-global mechanism were utilized. Finally, Tufano et al. [25] performed the most complete study up to date, in which all stages of the coal particle conversion are considered, i.e. heating, drying, ignition, volatiles combustion and char particle conversion. Moreover, in addition to detailed chemistry, their numerical model accounts for complex features of particle interior, such as time evolution of porosity and tortuosity. Most recently, Nguyen et al. [26] performed unsteady particle-resolved simulations to investigate the evolution of char particle morphology. Based on their results, improved expressions for the mode of burning and the Random Pore Model were proposed.

In the existing literature on resolved particle conversion, very different levels of numerical model complexity are presented. The current trend seems to be towards more and more detailed models and models that are able to capture transient effects. However, high accuracy is achieved at the expense of efficiency. The objective of this work is to propose a novel numerical approach for resolved char particle combustion modeling. Contrary to the present trend in the literature, we aim for the model to be as simple and efficient as possible, while still preserving high accuracy and being able to predict unsteady phenomena. This is accomplished by using structured, overset grids and by introducing carefully verified assumptions and simplifications.

2. Governing equations and numerical methods

An open-source, compressible solver called the Pencil Code [27] is used to perform the simulations presented in this work. The Pencil Code uses a 6th order finite difference scheme and a 3rd order Runge–Kutta scheme for spatial and temporal discretization, respectively. One of the main features of the numerical approach employed in this study is the overset grid. The particle is surrounded by a cylindrical body-fitted grid (later also referred to as 'ogrid'), which spans the space between $r = r_p$ to $r = 3r_p = r_{ogrid}$, where r is a radial coordinate and r_p is the particle radius. The rest of the computational domain is resolved on the Cartesian grid. Such an approach allows one to use very high resolution close to the particle, which is necessary to resolve its boundary layer and the surrounding flame. Further away from the particle, the grid is much coarser, making the computational effort relatively low. The solution is interpolated between the ogrid and the Cartesian grid using a 4th order, explicit Lagrangian interpolation method, which has been shown to be an optimal choice in connection with a 6th order finite difference scheme [28,29]. In order to avoid spurious oscillations, Padé filtering [30,31] is applied on the cylindrical grid to density, temperature and velocity fields. The details about the implementation of the overset grid and performance of this method can be found in [32,33].

2.1. Fluid equations

The continuity and momentum equations are solved in their non-conservative, compressible form:

$$\frac{\partial \rho}{\partial t} + \nabla \cdot (\rho \mathrm{u}) = 0, \tag{1}$$

$$\rho \frac{\partial \mathrm{u}}{\partial t} + \rho \mathrm{u} \cdot \nabla \mathrm{u} = -\nabla p + \nabla \cdot \underline{\underline{\tau}} + \boldsymbol{f}, \tag{2}$$

where ρ and p are the density and pressure, respectively, and the bold symbols represent the velocity (u) and volumetric force (f) vectors. The stress tensor, $\underline{\underline{\tau}}$, is given by

$$\underline{\underline{\tau}} = \mu(\nabla \mathrm{u} + (\nabla \mathrm{u})^T) - \frac{2}{3}\mu(\nabla \cdot \mathrm{u})\underline{\underline{\tau}}, \tag{3}$$

where μ stands for the dynamic viscosity and $\underline{\underline{\tau}}$ is the identity matrix. The mass fraction of chemical species k, given by Y_k, obeys the following transport equation

$$\rho \frac{\partial Y_k}{\partial t} + \rho \mathrm{u} \cdot \nabla Y_k = -\nabla \cdot \mathbb{J}_k + \dot{\omega}_k, \tag{4}$$

in which the diffusive flux, $\mathbb{J}_k$, is simplified by using the assumption of Fickian diffusion, such that

$$\mathbb{J}_k = -\rho D_k \nabla Y_k, \tag{5}$$

where D_k is the diffusion coefficient of species k and $\dot{\omega}_k$ represents the gas phase reaction rate of the same species.

By neglecting viscous heating, the energy equation is expressed in terms of temperature as [34]

$$\rho \frac{\partial T}{\partial t} + \rho \mathrm{u} \cdot \nabla T = \sum_k (\dot{\omega}_k - \nabla \cdot \mathbb{J}_k)\left(\frac{TR}{c_v M_k} - \frac{h_k}{c_v}\right) - \frac{\rho T R}{c_v M} \nabla \cdot \mathrm{u} - \frac{\nabla \cdot \mathbf{q}}{c_v}, \tag{6}$$

where T represents the temperature, c_v is the heat capacity at constant volume, R is the universal gas constant and M is the molar mass for the mixture, $1/M = \sum_k Y_k/M_k$. The heat flux, II, is computed as

$$\mathrm{II} = \sum_k h_k \mathbb{J}_k - \lambda \nabla T, \tag{7}$$

where λ represents thermal conductivity and $h_k = \Delta h_{s,k} + h^0_{f,k}$ is the absolute enthalpy of species k, which is the sum of its sensible enthalpy, $\Delta h_{s,k}$, and its heat of formation, $h^0_{f,k}$. Finally, to relate density with pressure, the ideal gas equation of state is used,

$$p = \frac{\rho R T}{M}. \tag{8}$$

2.2. Chemical mechanism and boundary conditions

A simplified chemical mechanism that consists of two surface reactions and one reversible gas phase reaction is employed:

$$2\mathrm{C} + \mathrm{O_2} \rightarrow 2\mathrm{CO} \tag{R1}$$

Table 1
Kinetic parameters. Here, $[a]$ denotes concentration of species a, k_i is given by Eq. (9) and r_i represents the rate-of-progress variable. Note that for surface reactions units of r_i are mol/cm^2/s, while for gas phase reactions it is mol/cm^3/s.

reaction	B_i	E_i[kcal/mol]	r_i	source
R1	1.97×10^9 cm / s	47.3	$k_1[O_2]$	[36]
R2	1.29×10^7 cm /s	45.6	$k_2[CO_2]$	[36]
R3 (forward)	3.98×10^{14} $(\frac{\text{cm}^3}{\text{mol}})^{3/4}$/s	40.7	$k_{3,f}[CO][H_2O]^{1/2}[O_2]^{1/4}$	[37]
R3 (reverse)	5×10^8 1/s	40.7	$k_{3,r}[CO_2]$	[37]

$$C + CO_2 \rightarrow 2CO \tag{R2}$$

$$CO + 0.5O_2 \leftrightarrow CO_2 \tag{R3}$$

It should be noted that the gasification reaction through H_2O is not considered in the present study, even though water vapor is present in the atmosphere. The reason this reaction was omitted was the very low concentration of H_2O ($Y_{H_2O} = 8 \times 10^{-4}$ at the inlet), which has been shown by Kestel et al. [15] to have essentially no effect on the conversion rate. To study cases characterized by higher content of water vapor, the additional gasification reaction and the water-gas shift reaction should be included in the mechanism. The Arrhenius expression for reaction i reads

$$k_i = B_i \exp(-E_i/RT). \tag{9}$$

The empirical kinetic parameters: pre-exponential factor B_i, activation energy E_i and reaction orders are listed in Table 1. The reaction term for the gas phase reaction in Eq. (4) is computed as

$$\dot{\omega}_k = M_k \sum_{i=1}^{n_{r,gas}} (\nu''_{ki} - \nu'_{ki}) r_i, \tag{10}$$

where ν'_{ki} and ν''_{ki} are the stoichiometric coefficients of gas phase species k in reaction i on the reactant and product side, respectively, while $n_{r,gas}$ is the number of gas phase reactions, and r_i is the rate-of-progress variable (adopting terminology from Ch. 4 in [35]), as given in Table 1.

Since the particle interior is not included in the current framework, it is assumed that all contributions to the reaction rate due to internal reactions are accounted for through the apparent kinetic parameters, and that the temperature gradient inside the particle is small enough to be neglected. Also, the particle is assumed to be entirely made of carbon and the model does not incorporate particle shrinkage during its conversion. In reality, the particle size and density are slowly changing as combustion progresses [38]. However, the typical time of our simulations is much shorter than the burnout time of the particle such that the reduction of the particle diameter can be considered negligible.

As stated above, the interior of the particle is not included in the computational mesh. The interaction between the solid and the surrounding gas is therefore incorporated through the particle boundary conditions. We will now continue by describing these boundary conditions. The species balance at the cylinder surface can be expressed as [6]:

$$\rho D_k \frac{\partial Y_k}{\partial r} + \dot{m}_c Y_k + \dot{m}_k = 0, \tag{11}$$

where

$$\dot{m}_k = M_k \sum_{i=1}^{n_{r,heter}} (\nu''_{ki} - \nu'_{ki}) r_i, \tag{12}$$

is the production rate of species k due to heterogeneous reactions, and $n_{r,heter}$ is the number of heterogeneous reactions. The char conversion rate is given by

$$\begin{aligned} \dot{m}_c &= -M_C(2k_1[O_2] + k_2[CO_2]) \\ &= -(\dot{m}_{O_2} + \dot{m}_{CO_2} + \dot{m}_{CO}) = -\sum_{k=1}^{n_{s,gas}} \dot{m}_k, \end{aligned} \tag{13}$$

where the final summation is over all gas-phase species. A detailed deduction of Eq. (11) can be found in Appendix A. It should be noted that both $\dot{m}_c$ and $\dot{m}_k$ depend on the species concentration on the surface, which makes it necessary to solve Eq. (11) in an iterative manner. Another possibility is to use species production rates from the previous time step, this can however lead to numerical instabilities and non-physical results. Here, we employ a simple iterative algorithm to simultaneously find solutions for Y_{O_2} and Y_{CO_2} at the surface, while the remaining species are solved for directly.

Mass conservation at the particle surface requires that (see Appendix A)

$$\sum_k (\rho Y_k \mathrm{u} + \mathbb{J}_k) \cdot \hat{\boldsymbol{r}} = \sum_k \dot{m}_k = -\dot{m}_c, \tag{14}$$

where $\hat{\boldsymbol{r}}$ is the vector normal to the particle surface. From the above equation, and since $\sum_k \mathbb{J}_k \cdot \hat{\boldsymbol{r}} = 0$, the boundary condition for velocity becomes:

$$u_r = -\dot{m}_c/\rho, \tag{15}$$

where u_r is the outward velocity in the radial direction, corresponding to the so called Stefan flow.

Dirichlet boundary condition is employed for the temperature. The intention behind the Dirichlet boundary condition for temperature is to validate the code against the experimental data of Makino et al. [39], where the temperature was maintained constant. The last variable that needs to be defined at the cylinder surface is density, which is solved for directly from the transport equation and does therefore not require any special treatment at the boundary.

2.3. Transport properties

In simulations of reacting flows, it is common practice to compute transport coefficients, such as μ_k, D_k and thermal diffusivity D_{th}, based on the kinetic theory of gases, as described e.g. in [34]. This approach, while accurate, significantly increases computational cost. This is especially the case for species diffusion coefficients for which binary diffusion coefficients need to be evaluated first. In order to maximize computational efficiency, a simplified approach is employed in this work. At the same time, care is taken not to compromise the accuracy of the results.

The kinetic viscosity is related to temperature through Sutherland's law

$$\nu = \frac{C_1 T^{3/2}}{\rho(T + C_2)} \tag{16}$$

with constants $C_1 = 1.52 \cdot 10^{-6}$ kg/m/s/K$^{1/2}$ and $C_2 = 110$ K. The above expression is fully applicable to single-component gases. However, if a mixture is dominated by components with similar

Table 2
Polynomial coefficients for heat capacity in the temperature range 1000 K $< T <$ 5000 K.

species	CO	CO_2	H_2O	N_2	O_2
a_1	3.025	4.454	2.672	2.927	3.698
a_2	$1.443 \cdot 10^{-3}$	$3.140 \cdot 10^{-3}$	$3.056 \cdot 10^{-3}$	$1.488 \cdot 10^{-3}$	$6.135 \cdot 10^{-4}$
a_3	$-5.631 \cdot 10^{-7}$	$-1.278 \cdot 10^{-6}$	$-8.730 \cdot 10^{-7}$	$-5.685 \cdot 10^{-7}$	$-1.259 \cdot 10^{-7}$
a_4	$1.019 \cdot 10^{-10}$	$2.394 \cdot 10^{-10}$	$1.201 \cdot 10^{-10}$	$1.010 \cdot 10^{-10}$	$1.775 \cdot 10^{-11}$
a_5	$-6.911 \cdot 10^{-15}$	$-1.669 \cdot 10^{-14}$	$-6.392 \cdot 10^{-15}$	$-6.753 \cdot 10^{-15}$	$-1.136 \cdot 10^{-15}$

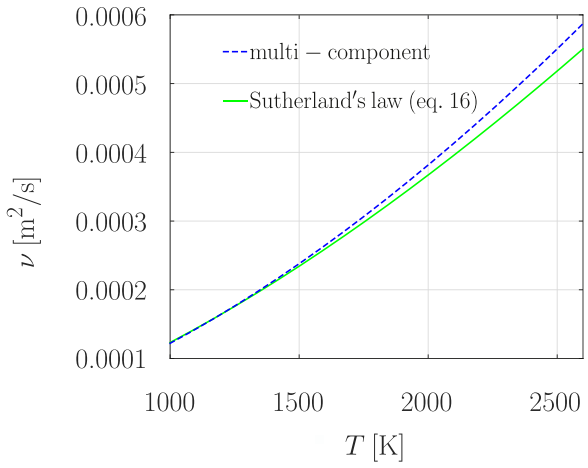

Fig. 1. Kinetic viscosity as obtained using Sutherland's law (Eq. (16)) and multi-component approach for the mixture consisting of $Y_{N_2} = 0.7292$, $Y_{O_2} = 0.05$, $Y_{H_2O} = 0.0008$, $Y_{CO} = 0.02$ and $Y_{CO_2} = 0.2$.

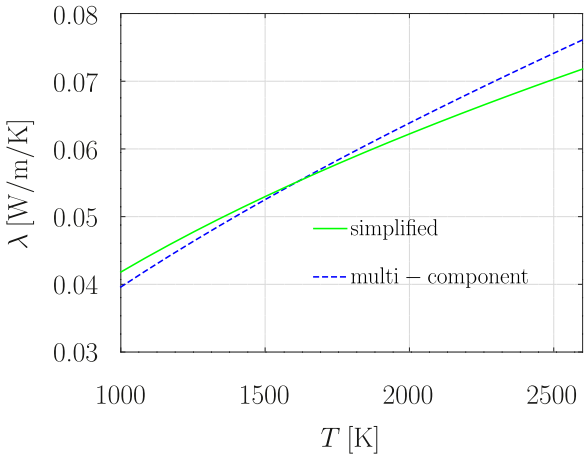

Fig. 2. Thermal conductivity as obtained using Eq. (17) with Pr = 0.9 and multi-component approach for the mixture consisting of $Y_{N_2} = 0.7292$, $Y_{O_2} = 0.05$, $Y_{H_2O} = 0.0008$, $Y_{CO} = 0.02$ and $Y_{CO_2} = 0.2$.

properties (as is the case here), Eq. (16) is reduced to a decent approximation. Furthermore, constants C_1 and C_2 were selected such that for a wide range of temperatures and compositions the kinetic viscosity resulting from Eq. (16) is in a good agreement with the kinetic viscosity determined using the multi-component approach (i.e. based on kinetic theory). In Fig. 1, these two methods are compared for a typical composition encountered in the current work. For other compositions that are likely to occur, a deviation from the kinetic theory remains below 7% for the temperature range presented in Fig. 1.

The main assumption allowing us to compute the remaining transport coefficients is that the transport coefficients are proportional to each other, i.e.

$$\nu = \mathrm{Pr} D_{th} = \mathrm{Pr} \mathrm{Le}_k D_k, \tag{17}$$

with the constants of proportionality being the Prandtl (Pr) and Lewis (Le_k) numbers. Such an assumption of constant Prandtl and/or Lewis numbers has successfully been applied in recent studies on resolved particle devolatilization and combustion [12,23]. Typically, Pr= 0.7 and $\mathrm{Le}_k = 1$ for all species are assumed. This was shown to have a negligible impact on the devolatilization stage when compared with the complex multi-component approach [12]. However, in some conditions, the combustion rate might be affected by diffusion coefficients, as will be demonstrated in the next section. Therefore, a more careful approach is employed, as described below.

The heat capacity at constant pressure is given by

$$c_p = \sum_k Y_k c_{p,k} = \frac{R}{M} \sum_k Y_k \sum_{i=1}^{5} a_i T^{i-1}, \tag{18}$$

where the polynomial coefficients a_i are taken from Gordon and Mcbride [40] and are listed in Table 2 for the relevant temperature range. The heat capacity at constant volume is related to the heat capacity at constant pressure through the gas constant, such that

$$c_p - c_v = R/M. \tag{19}$$

Using the heat capacity given by Eq. (18) and the thermal diffusivity given by Eq. (17), the thermal conductivity, defined as

$$\lambda = c_p \rho D_{\mathrm{th}}, \tag{20}$$

is shown in Fig. 2 as a function of temperature for the same mixture as used in Fig. 1. In Fig. 2, the thermal conductivity as obtained using the multi-component approach is also presented. The best agreement between these two functions for a wide range of mixtures is achieved by setting the Prandtl number equal to 0.9.

For each species, Le_k is chosen such that the resulting diffusion coefficient does not differ by more than around 10% from the diffusion coefficient computed based on the multi-component diffusion approach. This was verified for the full range of compositions and temperatures that are likely to appear in the cases we examine. Figure 3 presents a comparison between the diffusion coefficients as a function of temperature as computed from Eq. (17) and as obtained using the multi-component diffusion. The magnitudes of the Lewis numbers leading to these results are listed in Table 3. A good agreement between the two approaches is achieved for all transport coefficients (ν, λ and D_k), which justifies the use of the simplified approach for the transport coefficients.

Table 3
Selected Lewis numbers.

species	CO	CO_2	H_2O	N_2	O_2
Le_k	0.78	1.01	0.58	0.7	0.78

In order to quantify the efficiency gain obtained by simplifying the formulation of the transport coefficients, a one-dimensional flame was simulated for two cases (details regarding the one-dimensional flame simulations are given in the next section). In the first case, transport properties were computed according

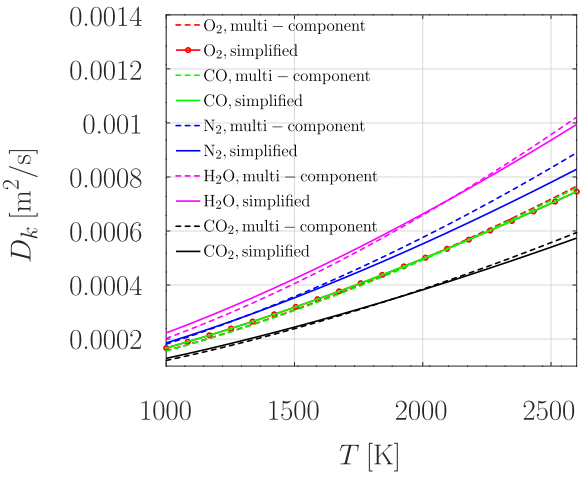

Fig. 3. Diffusion coefficients as obtained using Eq. (17) (referred to as 'simplified') and multi-component approach for the mixture consisting of $Y_{N_2} = 0.7292$, $Y_{O_2} = 0.05$, $Y_{H_2O} = 0.0008$, $Y_{CO} = 0.02$ and $Y_{CO_2} = 0.2$.

to Eqs. (16), (17) and (20), while in the second case, a multi-component approach was employed. A comparison of the execution time of subroutines responsible for computing transport properties revealed that 7.5 times less computational time was required for the case in which the simplified approach was used. Furthermore, since these subroutines are computationally the most expensive (i.e. their execution takes a large fraction of the simulation time), this corresponds to a reduction in the total execution time by a factor of 3.4. It should also be noted that the efficiency gain is dependent on the number of species present in the simulation. The reason for this is that one additional nested loop over all species must be executed and a significantly larger number of operations have to be performed to compute transport coefficients based on the kinetic theory. In our case, the factor of 7.5 was achieved for 5 species.

2.4. Speed of sound reduction

Numerical stability of the simulations requires several conditions to be fulfilled. First of all, a requirement due to convection, often called the CFL condition limits the maximum time step to:

$$\Delta t \leq \frac{C\Delta x}{\max(c_s + u)}, \tag{21}$$

where C is a constant that depends on a numerical scheme (typically $C \approx 1$) and

$$c_s = \sqrt{\gamma RT/M} \tag{22}$$

is the speed of sound and $\gamma = c_p/c_v$. For reacting flows, the length of the time step and the grid spacing is most often limited by chemical scales. However, it turns out that in the case of flows that are both reacting and compressible, the resolution requirement due to the ratio between viscosity and the speed of sound might be more restrictive. For the particular numerical approach employed in the Pencil Code, it has been shown [41] that the grid spacing is constrained by

$$\Delta x < \frac{\beta \nu}{c_s}, \tag{23}$$

where $\beta \sim 50$. It follows from Eq. (23) that larger grid spacing, and hence less mesh points, may be used if the speed of sound is reduced. A good rule of thumb is that, as long as we are not interested in thermo-acoustics, the results are independent of the Mach number, $\mathrm{Ma} = u/c_s$, for all Mach numbers below 0.1. In our case, the Mach number is typically of the order of 10^{-3}. The speed of sound can therefore be reduced by up to two orders of magnitude while still maintaining Mach-independent results. Since the time step is often limited by the CFL condition, which is typically the case for lower temperatures, a reduction of the speed of sound would also allow us to use larger time steps.

Table 4
Initial conditions for 1D carbon monoxide flame.

	reactant side	product side
Y_{O_2}	0.165	0.0
Y_{CO}	0.29	0.0
Y_{CO_2}	0.0	0.455
Y_{H_2O}	0.0008	0.0008
Y_{N_2}	0.544	0.544
T[K]	298	2000

In the previous paragraph we showed that a reduction in the speed of sound could be very beneficial for the CPU consumption of our simulations, and that the effect such a reduction has on the results should be negligible if the Mach number is kept below a certain value. The question now is how the speed of sound can be changed without affecting any other aspect of the results. This is done by dividing the gas constant by a factor α^2, such that

$$R \to R/\alpha^2, \tag{24}$$

which implies that (22)

$$c_s \to c_s/\alpha. \tag{25}$$

The gas constant is changed consistently for all equations, with the exception of Eq. (9) in which the original magnitude of R must be used in order for the reaction rate not to be affected. It should be noted that the reduction of R means that c_p, c_v and λ are also reduced by the same factor of α^2, as can be seen from Eqs. (19) to (20). However, this has no effect on the energy equation as all these reductions cancel out in every term of Eq. (6). The only term that is affected is the pressure gradient term in the momentum equation, since $\nabla p \sim c_s^2$, which is as intended.

We will now validate the assumption that a reduction in the speed of sound does not affect the main results, except for the acoustic waves, as long as the Mach number is below 0.1. This is done by simulating reacting flows of a one-dimensional carbon monoxide flame with three different values of c_s. In the base case, the speed of sound was kept unchanged, which resulted in $\mathrm{Ma} \approx 0.001$, in the other cases the speed of sound was reduced by factors of 10 and 50, which led to $\mathrm{Ma} \approx 0.01$ and $\mathrm{Ma} \approx 0.05$, respectively. The initial conditions for these cases are given in Table 4, while the one-step mechanism given in Section 2.2 governs the flame.

The resulting temperature and species mass fraction profiles at steady state are presented in Fig. 4, from which it can be seen that the results are not affected by the speed of sound reduction. Furthermore, for all three cases, the same flame speed, $S_L = 14\,\mathrm{cm/s}$, is obtained. Having verified that the speed of sound can be reduced without affecting the results, this tactic is employed for all cases discussed in the next section, which resulted in a major reduction of CPU power consumption, in particular for those cases where the time-step was not limited by chemical reactions. It is also worth mentioning that the efficiency gain resulting from the speed of sound reduction is very case-dependent. This can be illustrated by subsequently reducing the spatial resolution of the 1D flame simulation in which the speed of sound was reduced by a factor of 10 (corresponding to the green line in Fig. 4). Despite the fact that the maximum grid size, as defined by Eq. (23), is inversely proportional to the speed of sound, it was possible to reduce the resolution only by a factor of ~3 due to the fact that, for stability rea-

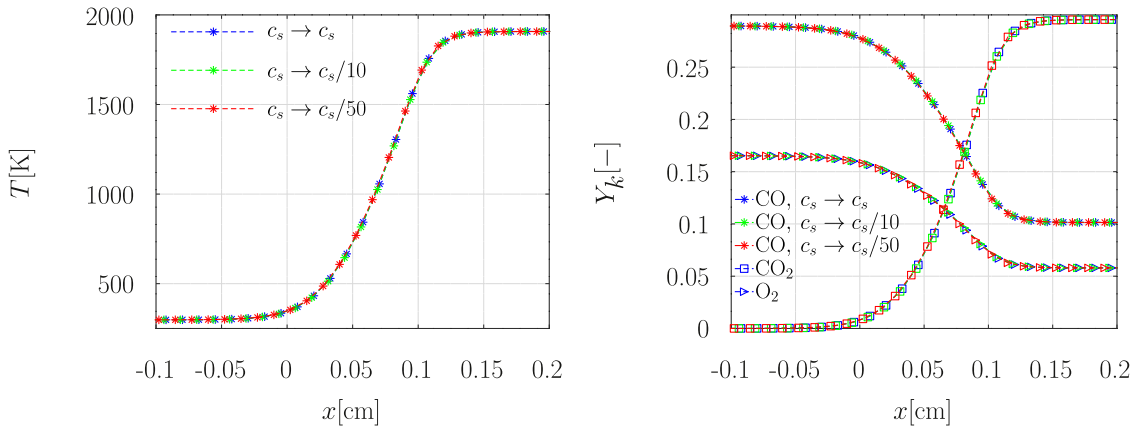

Fig. 4. Comparison of temperature and species profiles across the flame obtained before and after the speed of sound reduction. (For interpretation of the references to color in this figure legend, the reader is referred to the web version of this article.)

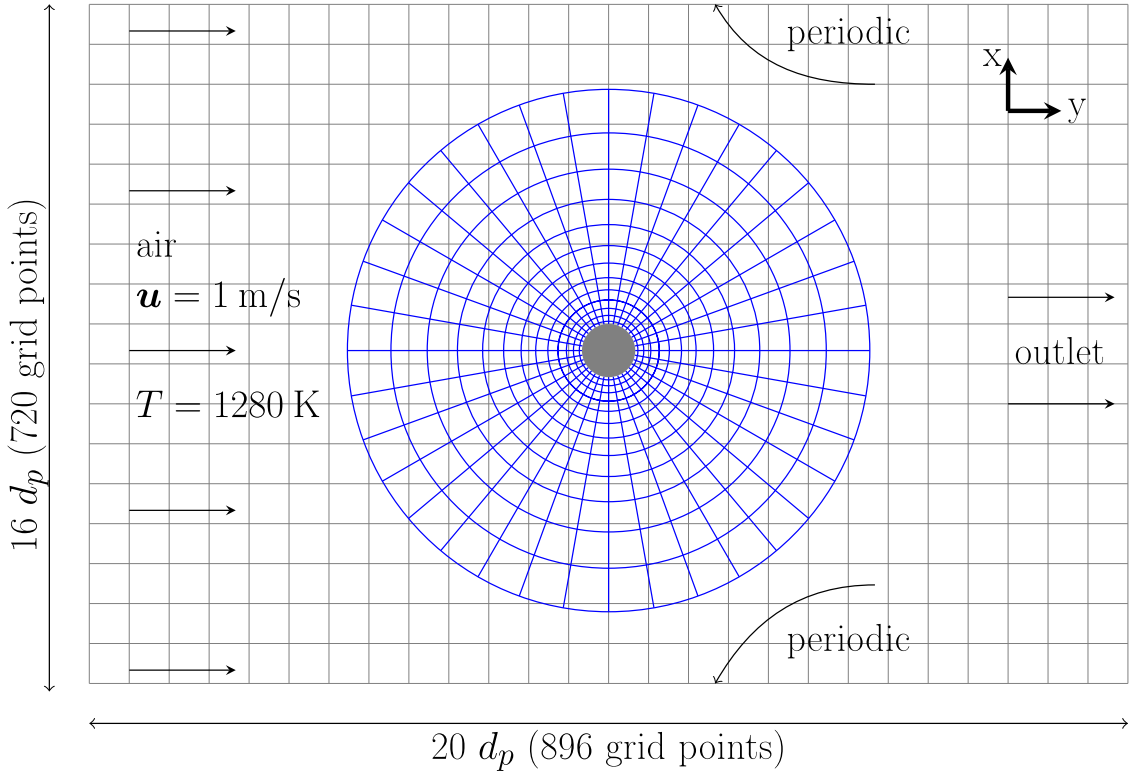

Fig. 5. Schematic representation of the analyzed case (not drawn to scale).

sons, a certain number of grid points are required across the flame front. It can be therefore concluded, that the speed of sound reduction allows one to eliminate the grid size/time step requirement due to the speed of sound in low Mach number flows, but the efficiency gain associated with this cannot be quantified in general basis since it depends on other case-specific time and length scales.

2.5. Numerical set-up

The set-up for all simulated cases correspond to the experimental set-up of Makino et al. [39] and can be summarized as follows. A cylindrical particle of 5 mm in diameter is placed in the middle of a 10 cm × 8 cm computational domain. The fluid, which has a composition that is typical for air ($Y_{N_2} = 0.77$, $Y_{O_2} = 0.23$, $Y_{H_2O} = 0.0008$) enters the domain through one side with a velocity of 1 m/s in the $y-$direction. Periodic boundary conditions are specified in the two cross-flow directions. Initially, the temperature inside the domain is everywhere equal to 1280 K. The initial species distribution on the ogrid is such that the oxygen mass fraction decreases exponentially from $Y_{O_2} = 0.23$ at $r = r_{ogrid}$ to $Y_{O_2} = 0$ at the particle surface ($r = r_p$), while carbon dioxide is introduced in place of oxygen, *i.e.* $Y_{CO_2}(r) = Y_{O_2}(r_{ogrid}) - Y_{O_2}(r)$. The initial composition on the Cartesian grid is the same as the composition at the inlet. Such initial conditions do not reflect the experimental set-up and were selected purely to improve stability of simulations during the initial stage.

For most cases, a grid resolution of 720 x 896 (x x y directions) grid points on the Cartesian grid and 208 x 432 (r x θ directions) on the ogrid was sufficient to accurately resolve all flow features. It should be noted that the ogrid is stretched in a non-linear manner in the radial direction. For the resolution given

above this resulted in $\Delta r_{\min} = 8.3 \cdot 10^{-4}$ cm at the particle surface and $\Delta r_{\max} = 6.8 \cdot 10^{-3}$ cm at the outer edge of the cylindrical grid. A schematic representation of the numerical grid together with initial condition is presented in Fig. 5. If the particle temperature is relatively low ($T_p \lesssim 1800$ K) the maximum time-step is limited to $\sim 10^{-7}$ s by convection, while for higher particle temperatures the time-step needs to be reduced to $\sim 10^{-8}$ s due to the shorter chemical timescales.

3. Results and discussion

3.1. Implementation of chemistry module - validation

Various aspects of the Pencil Code have been validated and tested a number of times and the results have been published in a large number of papers available in the open literature. See [27] for an overview of some relevant papers. In this work, we have, however, implemented several new methods and approximations to speed up the calculations, such as: simplified calculation of transport data, simplified global reaction mechanisms, heterogeneous reactions at the particle surface with the overset grid method, and variable speed of sound. In order to validate the current numerical model beyond the more specific validations presented in the previous section, the experimental set-up of Makino et al. [39] is reproduced numerically. In the experiment of Makino et al., combustion of a graphite rod was studied at different surface temperatures, for different air velocities and temperatures. An important feature of the experiment is that the heat loss from the graphite surface due to radiation is balanced by electrical heating, such that a constant particle surface temperature is maintained at all times. As a result, a quasi-steady state is achieved for a relatively large fraction of the particle conversion time. In the current work, the case characterized by an air temperature of 1280 K and a velocity of 102.5 cm/s is analyzed for a range of particle surface temperatures. This particular selection of experimental conditions was motivated by the fact that the same case was studied numerically by Luo et al. [6], who demonstrated that a good agreement with the experimental results can be obtained using the chemical mechanism given by reactions (R1)–(R3). Despite the fact that Luo et al. also used the Pencil Code, there are two main differences between their approach and the approach used in the current work: (1) Luo et al. used kinetic theory to compute transport coefficients, and (2) their particle was resolved on a Cartesian grid using immersed boundary conditions for the particle surface.

Figure 6 presents the carbon conversion rate obtained with the current numerical approach (green squares) in addition to what was found experimentally by Makino et al. [39] (red circles) and numerically by Luo et al. [6] (blue circles). In fact, what is shown is the conversion rate in the forward stagnation point. Additionally, kinetic (solid blue line) and diffusion (dotted black line) limits for oxidation are also included in Fig. 6. The first limit corresponds to the case of infinitely fast diffusion ($Y_{O_{2,surface}} = Y_{O_{2,\infty}}$), while the latter to the reaction rate being controlled by diffusion ($\sim T^{1/2}$). It can be seen that up to $T_p = 1200$ K, the carbon conversion rate is governed by kinetics, while around $T_p = 1600$ K the slope corresponding to the diffusion limit is achieved. There is one more limiting slope included in Fig. 6, which is called 'flame diffusion' limit. This limit arises due to the fact that at around $T_p = 1700$ K the flame begins to detach from the particle surface. The reason for this detachment is the large CO production at the surface and its subsequent transport by means of the Stefan flow and diffusion. The result is that most of the O_2 is consumed in the gas phase at the position of the flame that is formed away from the surface. As a consequence, mostly CO_2 can diffuse to the surface and the carbon conversion is due to the Boudouard reaction (R2). From the perspective of the oxidation reaction, the oxygen diffuses

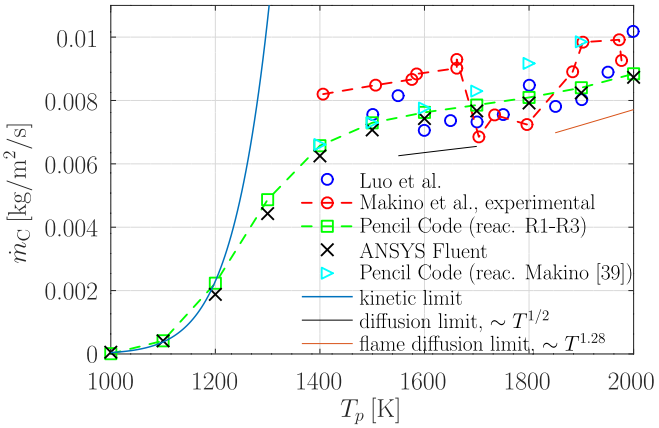

Fig. 6. Comparison of carbon conversion rates as a function of particle surface temperature. The results for Luo et al. [6] are reproduced from their Fig. 8. (For interpretation of the references to color in this figure legend, the reader is referred to the web version of this article.)

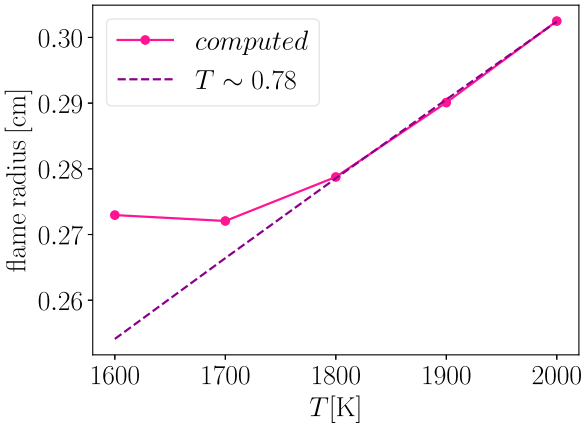

Fig. 7. Effective flame radius in a function of temperature.

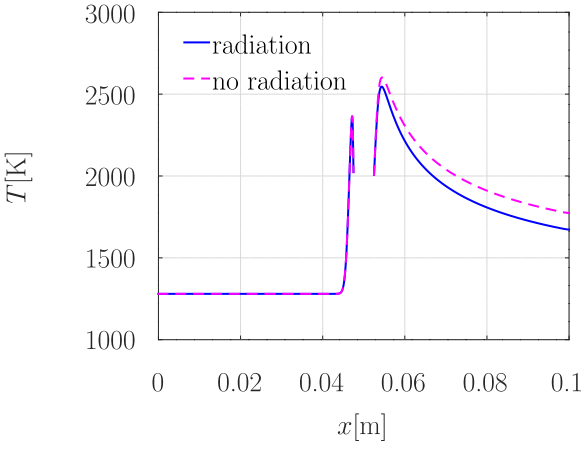

Fig. 8. Comparison of temperature profiles along the centerline with and without gas-to-gas radiation model.

now towards the flame surface, not the particle surface. This effective surface grows proportionally to T^g, where the exponent g can be found by a fitting procedure. This was done in Fig. 7, from which it can be seen that the 'effective radius' scales as $T^{0.78}$. Here, the effective radius was computed as the average radial distance from the particle center to the flame, where it was assumed that the flame location corresponds to the grid point in which the gas phase reaction rate is the highest. The carbon conversion rate in

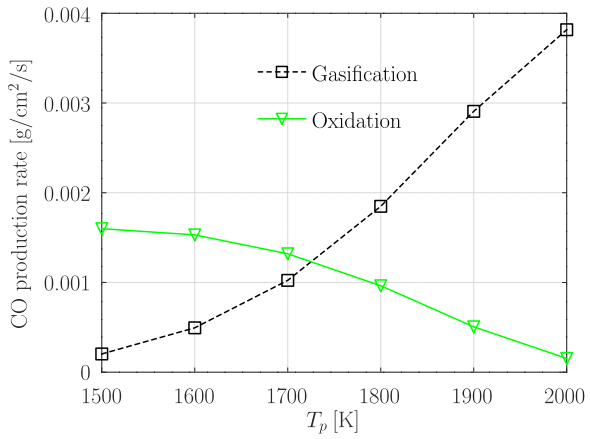

Fig. 9. Contributions to CO production from gasification and oxidation.

the diffusion limit is proportional to the product of the mass transfer coefficient (k_i) and the effective surface:

$$\dot{m}_c \sim d_{p,eff}^2 k_i, \tag{26}$$

where $d_{p,eff}$ is the effective diameter of the flame surface. Since the mass transfer coefficient scales as $k_i \sim D_i/d_{p,eff}$ and $D_i \sim T^{1/2}$ (see Eqs. (16) and (17)), the conversion rate dependence on temperature becomes:

$$\dot{m}_c \sim d_{p,eff}^2 k_i \sim d_{p,eff} D_i \sim T^{1/2} T^{0.78} = T^{1.28}. \tag{27}$$

This is the flame diffusion limit seen in Fig. 6, which is reached for the highest of the studied particle surface temperatures.

Compared to the experimental results, slightly too low conversion is obtained for most temperatures. On the other hand, very similar magnitudes of conversion rates were obtained by Luo et al. [6], which indicates that the difference is most probably caused by the reaction kinetics. It is in fact common that there is no agreement on the reaction kinetics and quite often a number of mechanisms are suggested, resulting in different reaction rates. The influence of heterogeneous kinetics has already been investigated by Nikrityuk et al. [42], who revealed that a factor of 2 or even 3 difference in the carbon consumption rate can be expected between different sets of kinetic parameters that are found in the literature. A set of kinetic parameters for surface reactions was also proposed by Makino et al. [39] based on their experimental results and the conversion rates resulting from these parameters are presented in Fig. 6 (cyan triangles). It can be seen that this yielded a significantly higher carbon conversion rate at high surface temperatures, but did not lead to noticeable difference for $T_p \leq 1600$ K. This could be expected as the gasification reaction is much faster in Makino's mechanism, while there is only a tiny difference in the oxidation rates when compared with the mechanism given in Table 1.

Another experimental feature that is not captured properly with the current approach is a sudden decrease of the conversion rate for surface temperatures around 1700–1800 K. This decrease is also present in the results shown in Fig. 6 in Luo et al. [6] (although the results in their Figs. 6 and 8 seem to be inconsistent regarding this feature). The main difference between their and the present numerical approach is how the transport coefficients are computed. In that respect, our approach is much simpler and, potentially, less accurate. Therefore, a further validation is essential. Such a validation was performed using the ANSYS Fluent software, in which the same cases were reproduced and the resulting carbon conversion rates are shown as black x-signs in Fig. 6 [add contours here or a plot showing T comparison along centerline]. The Fluent simulations were performed with the diffusion coefficients calculated from kinetic theory, as was also done by Luo et al. [6]. In addition, incompressible and steady state flow was assumed. Both assumptions are valid since the Mach number is low and the change in particle radius is very slow. As can be seen in Fig. 6, almost the same conversion rates were obtained using the complex formulation for the transport coefficients in ANSYS Fluent as for the simplified formulation used in the Pencil Code. In particular, the conversion rates in both cases are monotonically increasing functions, i.e. no reduction of the conversion rate was observed around $T_p =$ 1700–1800 K. This verifies that the simplified approach for the transport is not responsible for this qualitative discrepancy between the experimental results and our numerical results, and allows us to gain confidence in the predictions of our approach.

The case that was set up in ANSYS Fluent was also used to estimate the influence of gas phase radiation, which was omitted in the energy equation in the Pencil Code. While it is not uncommon to omit gas-to-gas radiation in simulations of conversion of resolved char particles, some studies suggest that its effect is non-negligible. For example, a significant reduction of the char particle surface temperature due to gas phase radiation was observed by Richter et al. [16], especially for cases with high ambient temperature. On the other hand, Tufano et al. [12] showed that the effect of gas-to-gas radiation on ignition is rather weak. In our study, the gas phase radiation was accounted for through the Discrete Ordinates model, and its influence can be seen in Fig. 8, which compares the temperature distribution along the centerline of the reacting particle for the cases with and without radiation. The case with $T_p = 2000$ K is shown here since the effect of radiation is the highest for cases with high particle temperature. It can be seen that the effect on the gas phase temperature field is certainly non-negligible in the region behind the particle. Nevertheless, the conversion rate remained unchanged due to the experiment-imitating assumption of constant temperature at the particle surface and virtually no influence of radiation on species concentrations. It should be noted, however, that based on the results presented by Luo et al. [6], it is expected that the particle surface temperature is unlikely to change by more than a few percent for the cases studied in the present paper, even if heat transfer at the particle surface (chemical heat release, conduction, convection and radiation) was accounted for through the particle boundary condition.

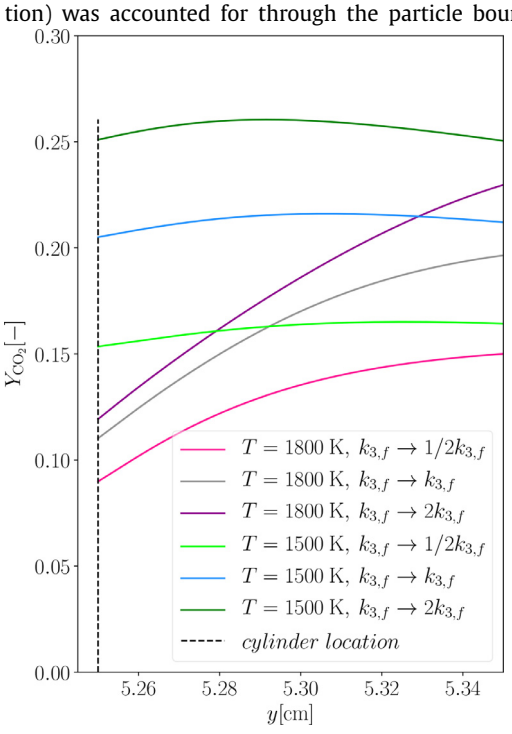

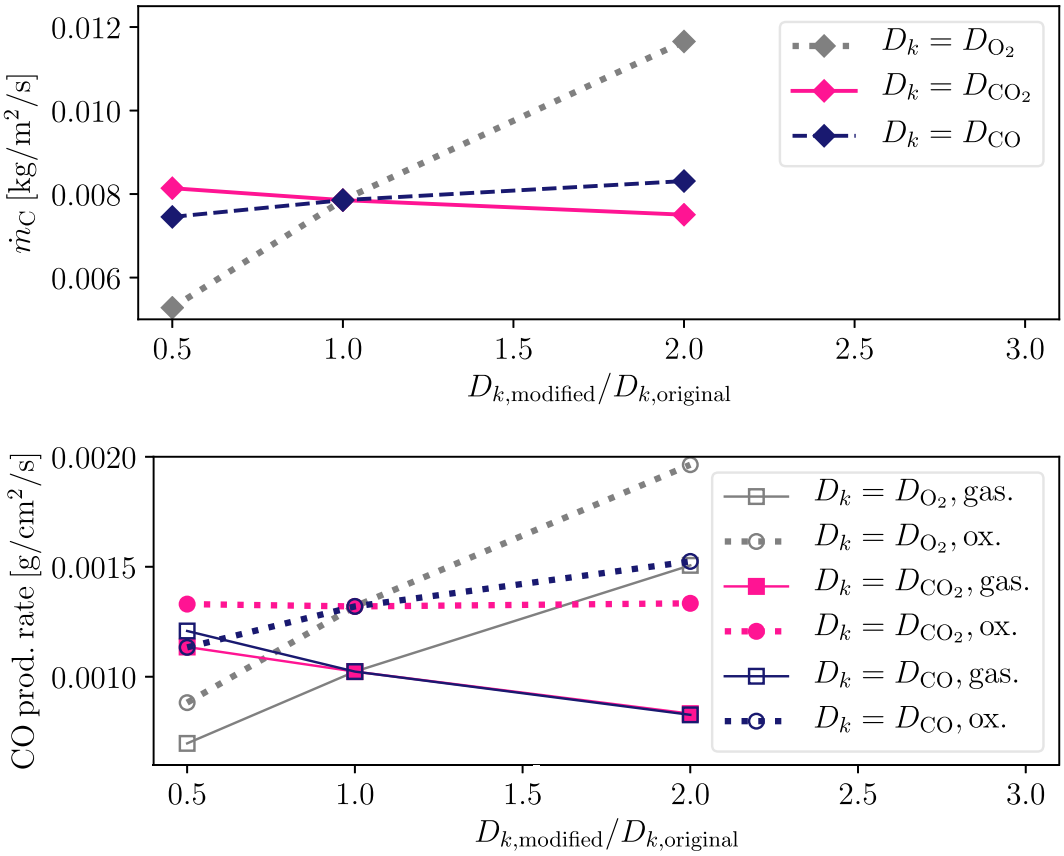

Fig. 10. Upper: conversion rates for different diffusion coefficients, lower: contributions from gasification/oxidation to the CO production rate, $T_p = 1700$ K.

It still remains to be understood why conversion rate obtained with the Pencil Code (and ANSYS Fluent) does not follow the experimental trend when it comes to the dip in carbon conversion rate around $T_p = 1700$ K. There exist several physical explanations of this trend in the literature, e.g.: it is attributed to the change of the effective reaction zone thickness [43], it is linked with the change of molecular structure of graphite [44,45], it is caused by thermal rearrangement of surface-covering sites, from highly reactive at low temperatures to less reactive at higher temperatures [46,47]. Makino et al. [39] argue that the presence of the dip stems from the fact that the dominant surface reaction shifts from oxidation to gasification around $T_p = 1700$ K. The reason for this shift is that at low temperatures the oxygen is used to oxidize the carbon directly at the surface, while at high temperatures the oxygen is used to oxidize CO in a CO-flame surrounding the particle, while the carbon conversion proceeds through gasification of CO_2 that diffuse to the surface from the CO flame. This change in the dominant mechanism for CO production at the surface is correctly predicted by the Pencil Code, as can be seen in Fig. 9. However, the shift is gradual and does not result in the non-monotonicity of $\dot{m}_C(T_p)$ as suggested by Makino et al. [39]. Another plausible explanation for the dip in $\dot{m}_c$ is that since the shape of the conversion function depends on the gas phase kinetics, as shown in [48], the kinetic parameters we use might not yield the right behavior. While all the above explanations are probable, it is also possible that the results are affected by the measurement method. In the experiment, the surface temperature of the rod was measured using two-color pyrometer [49]. These measurements are used to control the internal heating that is required to maintain a constant temperature of the graphite rod. This method is indirect, it might therefore be difficult to precisely measure the surface temperature without the results being affected by the surrounding flame. At relatively low surface temperatures, the flame remains attached to the surface, so the difference between the flame and the surface temperature is small. However, at temperatures at which the drop in the conversion rate is observed, the flame starts detaching from the rod surface. As such, the flame temperature might be significantly higher, giving a false impression of higher surface temperature. Since the experiment attempts to maintain a constant surface temperature, it is likely that the rod was cooled to lower temperature than intended, which resulted in a sudden decrease of the conversion rate. These are, however, only conjectures, and the reason for the qualitative inconsistency between the experiment and our results might be a combination of several of the above-mentioned factors.

3.2. Sensitivity analysis

In order to better understand which parameters that control the carbon conversion rate, we have done a series of parameter studies. The first study investigates the effect of species diffusivity. In this respect we varied the diffusivities of O_2, CO_2 and CO from half of their original value up to twice the original value, and investigated how this influenced the solid (carbon) conversion rate. For this investigation, we concentrate on the situation where the particle temperature is 1700 K.

From the upper panel of Fig. 10 we see that the solid conversion rate has a strong dependence on diffusivity of O_2. This is expected since higher diffusivity of O_2 will yield a higher transport rate of O_2 to the solid, which will then be able to convert (oxidize) more solid. From the lower panel of Fig. 10 we see that increasing the oxygen diffusivity results in an increase of both the oxidation and gasification rates of the solid. At first glance, it may look surprising that even the gasification rate increases with increased O_2

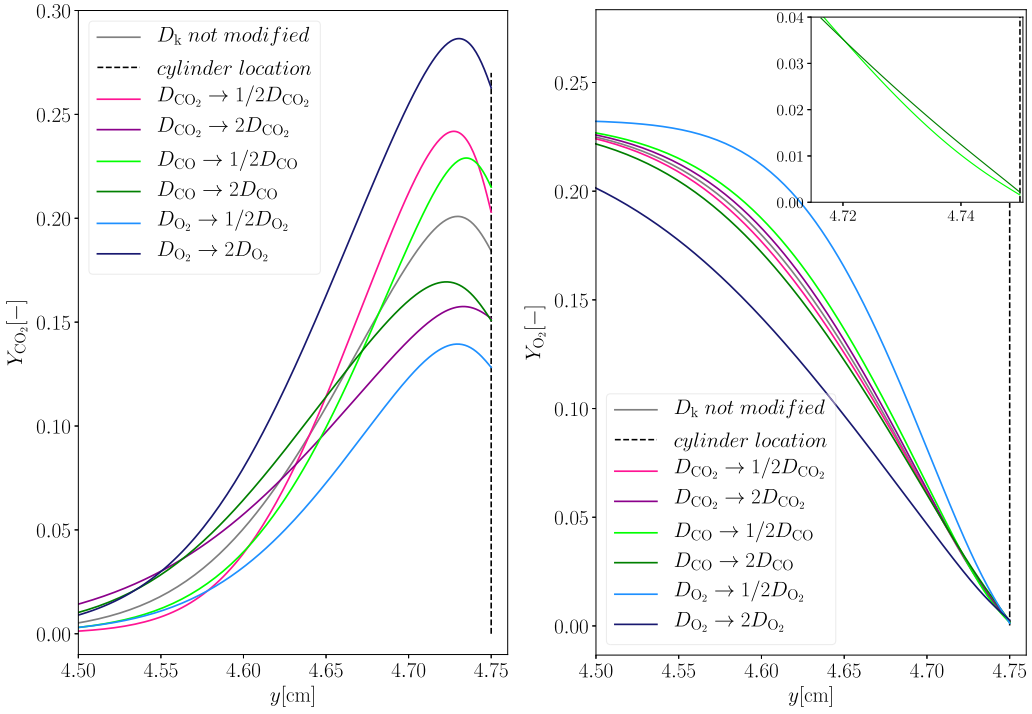

Fig. 11. Oxygen and carbon dioxide mass fractions and temperature profiles in the particle stagnation region as obtained for different diffusion coefficients.

diffusivity, but the reason is simply that at the surface temperature of 1700 K that we focus on here, we experience a higher surface-fraction of CO_2, resulting from oxidation of CO very close to the surface.

Let us now move on to the effect of CO diffusivity. We see from the upper panel of Fig. 10 that the solid conversion rate is weakly increasing with increasing diffusivity of CO. This effect is, however, more complicated than that of O_2 diffusivity, as can be seen from the lower panel of Fig. 10, which shows that solid conversion due to oxidation increases with CO diffusivity, while the opposite is true for gasification. To elucidate this behaviour in Fig. 11, we show CO_2 and O_2 concentrations along the y-axis in front of the solid. The dashed vertical line in the figure corresponds to the solid surface. From the left panel we see that lower CO diffusivity yields higher concentration of CO_2 at the surface, which explains why the gasification rate decreases with increasing CO diffusivity. The reason for the increased CO_2 concentration at the surface is that a lower CO diffusivity moves the flame closer to the surface. Since the CO_2 concentration is highest close to where it is produced, which is in the CO flame, this means that the concentration of CO_2 at the surface is also higher. Studying the gradients of O_2 very close to the surface (right panel) we see that the case with higher CO diffusivity has a steeper gradient of O_2 very close to the surface. For a given O_2 diffusivity, a steeper O_2 gradient results in more transport of O_2 to the surface, and, hence, more solid oxidation.

Finally, when increasing the diffusivity of CO_2, we see from Fig. 10 that the solid conversion rate is actually reduced. This is despite the fact that the solid oxidation rate is independent of the diffusivity of CO_2 (see the lower panel of Fig. 10). The question is therefore why the solid gasification rate is reduced when the CO_2 diffusivity is increased. The answer to that question is that for the current case, which has a solid temperature of 1700 K, the CO_2 is always produced close to the solid surface due to the CO flame not being significantly lifted. Consequently, an increased CO_2 diffusivity will tend to transport CO_2 away from the surface, lowering the surface concentration, and, by that, reducing the gasification rate.

Another parameter that can influence the carbon conversion rate is chemical kinetics, both of surface and gas phase reactions. In the following we will proceed by studying the sensitivity of the carbon conversion rate to the chemical reactivity. The reactivity is varied by changing the pre-exponential factor. First, the surface reaction rate is varied. This is done separately for the oxidation (denoted by $R1$) and gasification (denoted by $R2$) reactions. The effect of this variation on the conversion rate can be seen in Fig. 12 for two different surface temperatures: 1200 and 1800 K.

For the higher temperature, the conversion rate is almost uninfluenced by changes in the oxidation rate, which is due to the fact that at such high temperatures the reaction is controlled almost purely by diffusion. This is confirmed in the lower panel of Fig. 12, which shows that the oxidation rate (R1) variations have no effect neither on the contribution from oxidation, nor on the contribution from gasification. At the same surface temperature, variations in the gasification rate (R2) have only a weak effect on the solid conversion rate. However, the reason for this is quite different, as in this case both contributions from gasification and oxidation are significantly affected, as can be observed in the lower panel of Fig. 12. These two contributions are affected in such a way that the increase in the carbon conversion rate due to the higher gasification rate is almost exactly balanced by the decrease in the solid conversion rate due to the faster oxidation.

For $T_p = 1200$ K, the carbon conversion rate is directly proportional to the change of the oxidation rate (R1), but does not depend on the gasification rate (R2). This is expected since at this temperature the surface reaction rates are controlled by kinetics, but the contribution to the solid conversion rate from gasification is around two orders of magnitude smaller than the contribution from oxidation.

The effect of the gas phase kinetics is shown in Fig. 13, from which it is clear that the solid conversion rate is not sensitive to the gas phase reaction rate variations, as long as the surface reactions are controlled by kinetics, i.e. for $T_p = 1200$ K. At higher particle surface temperatures, the solid conversion becomes faster upon decreasing the gas phase reaction rate. This is consistent

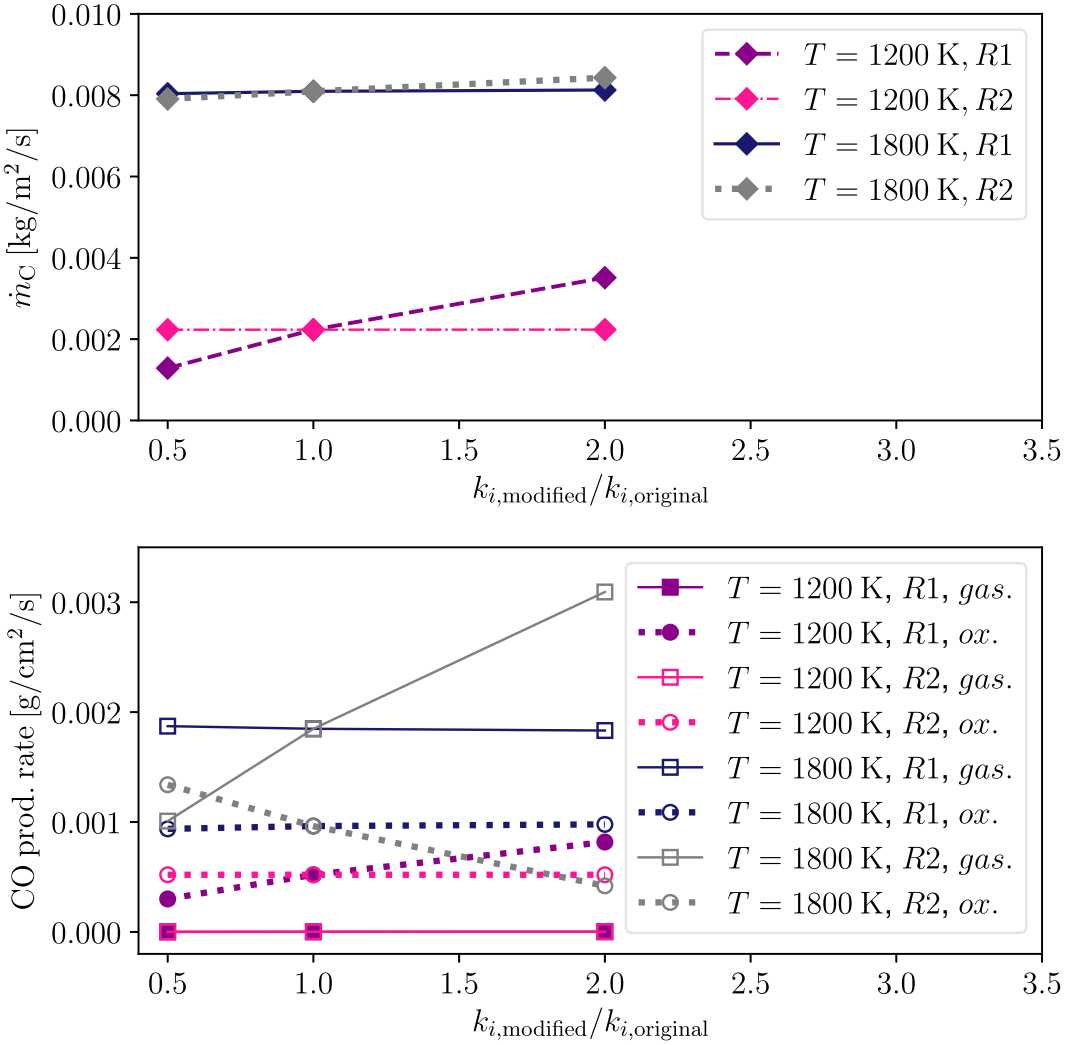

Fig. 12. upper: conversion rates as obtained for modified surface reaction rates, lower: contributions from gasification/oxidation to the CO production rate. *R*1 and *R*2 denote oxidation and gasification, respectively, and indicate which reaction has been modified, while ox. and gas. denote contribution from oxidation and gasification to the CO production rate.

with theoretical predictions of Libby and Blake [50] and Makino [51] who showed that the solid conversion rate is highest in the limit of the gas phase reaction rate approaching zero (so called 'frozen mode'), and lowest in the limit of very fast homogeneous reaction rate. This tendency can be linked to the fact that the higher the gas phase reaction rate, the more oxygen is consumed inside the CO-flame before reaching the particle surface, thus, the contribution to the combustion rate from oxidation decreases (see the lower panel of Fig. 13). Furthermore, the flame characteristics are also directly linked to the gas phase reaction rate. In particular, when the rate is increased, the flame becomes thinner and can detach from the particle surface or shift further from the surface if it was already detached. This situation can be observed in Fig. 14, which presents contours of the CO flame for the cases in

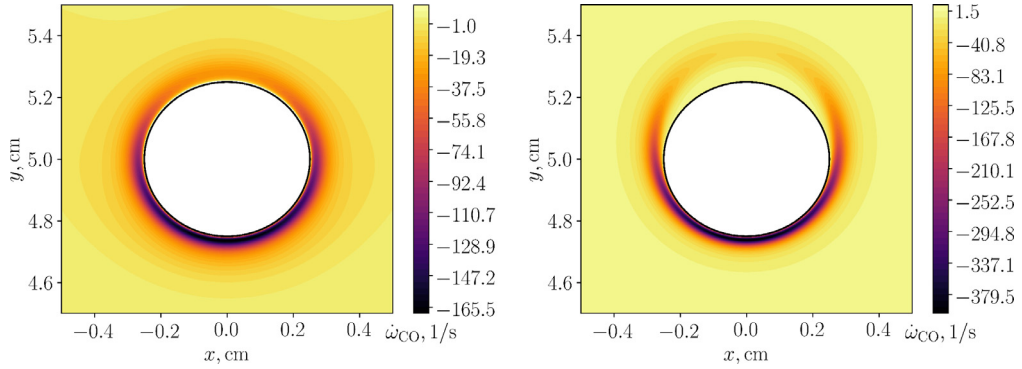

Fig. 14. CO flame contours, $T_p = 1800$ K, left: $k_{3,f} \rightarrow 0.5k_{3,f}$, right: $k_{3,f} \rightarrow 2k_{3,f}$.

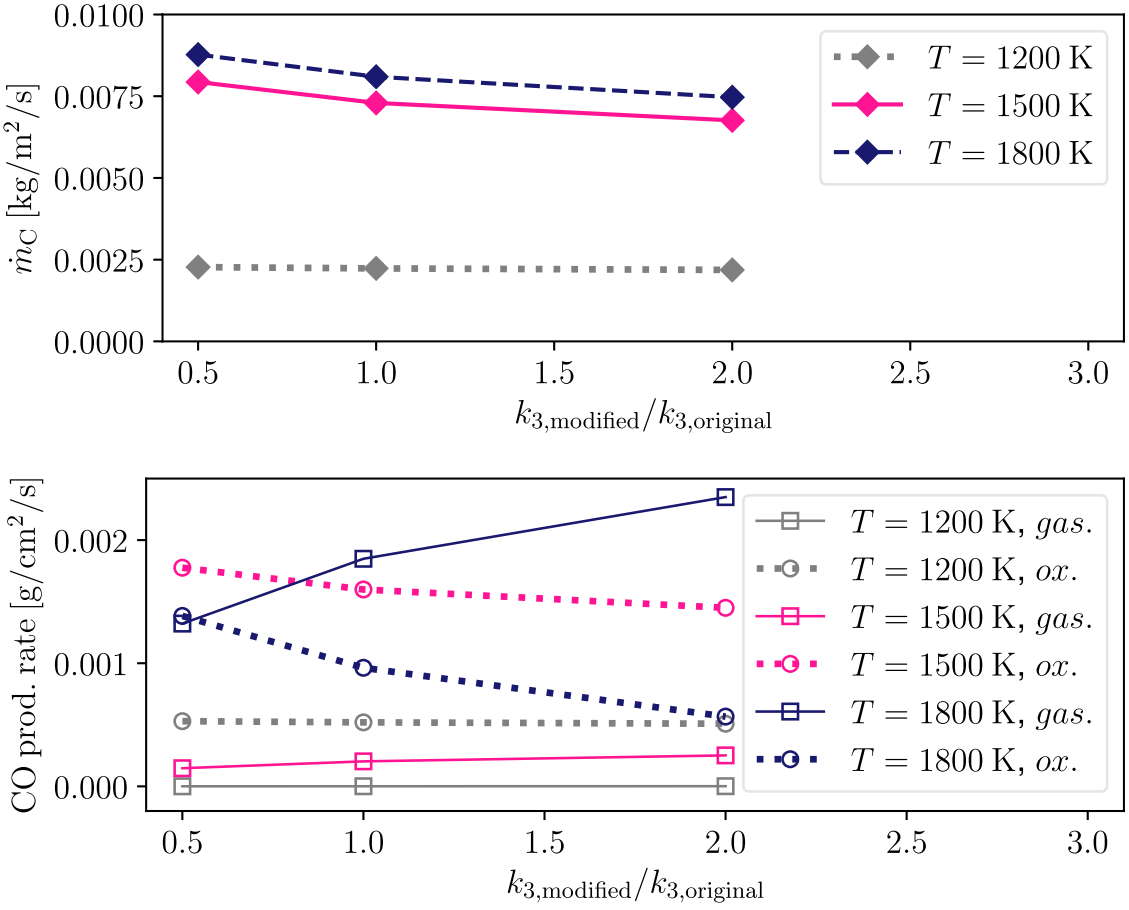

Fig. 13. upper: conversion rates as obtained for modified homogeneous reaction rate, lower: contributions from gasification/oxidation to the CO production rate.

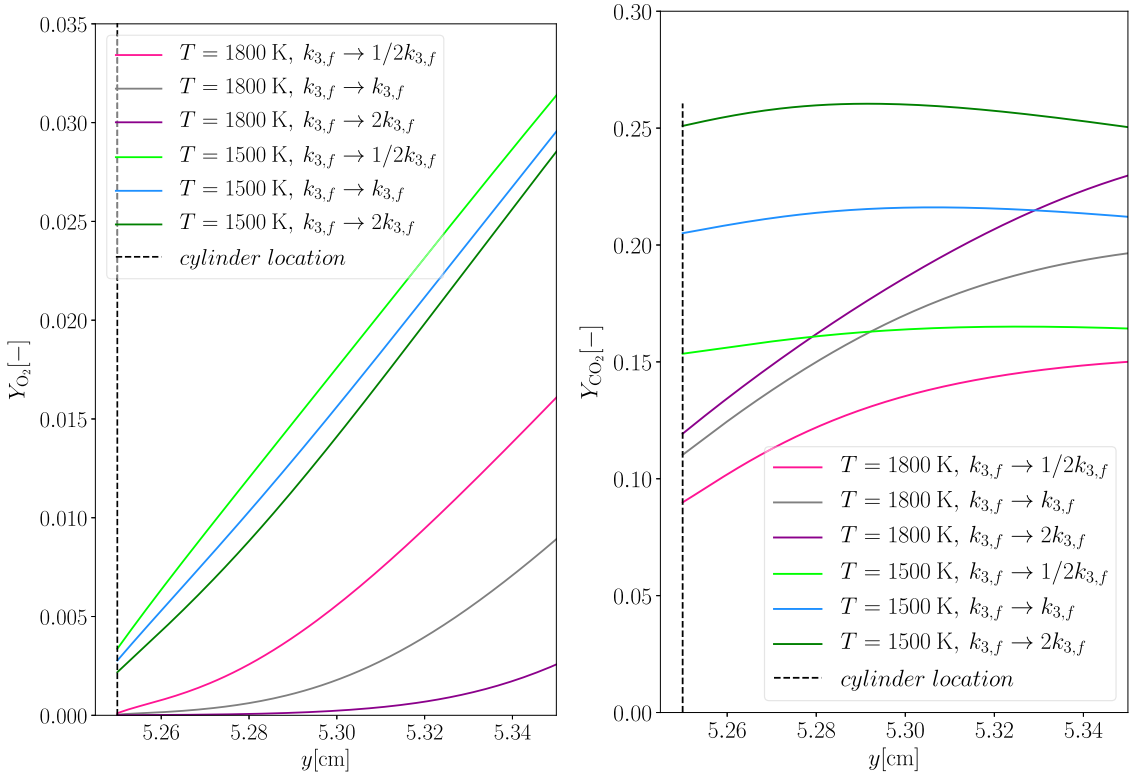

Fig. 15. Oxygen and carbon dioxide mass fraction profiles along the centerline behind the particle as obtained for different gas phase reaction rates.

which the pre-exponential factor of the homogeneous reaction rate was halved and doubled relative to what it was originally. A consequence of the flame moving away from the solid surface is that the gradient of oxygen between the flame and the surface becomes less steep, leading to a slower diffusion of O_2 towards the particle. This can be observed for $T_p = 1800$ K in Fig. 15, which shows oxygen profiles along the centerline behind the particle. For $T_p = 1500$ K, the flame is much closer to the solid surface, thus the oxygen profiles further away are almost parallel to each other, and the contribution to the combustion rate from oxidation is affected to a smaller extent, as seen in the lower panel of Fig. 13. The situation is opposite for carbon dioxide, as higher rate of homogeneous reaction means more CO_2 that is produced inside the flame and faster diffusion of this species to the surface. It is also interesting to notice in the right panel of Fig. 15 that for $T_p = 1500$ K the concentration of CO_2 at the solid surface is almost the same as the concentration inside the flame, which indicates that the gasification rate is still controlled by kinetics. Therefore, the increase of the contribution from gasification is simply caused by the higher mass fraction of CO_2 at the surface, not by the diffusion rate as was the case for $T_p = 1800$ K.

4. Conclusions

The goal of this work was twofold, first to formulate an efficient approach to model resolved solid particle combustion, then to understand the relevant physics and sensitivity. For this purpose, a model within the framework of the Pencil Code was developed and validated against experimental and numerical data. Our model is not as advanced as some approaches proposed in the literature, but it has a great potential to capture the transient nature of char conversion upon further development. Although within this study the laminar flow over a single particle was analyzed, the model can also be employed in turbulent flow situations. In order to achieve high efficiency, an overset grid was used, which allowed us to reduce the computational expense without compromising the accuracy. Other features of the numerical approach that have been proposed for the sake of efficiency are the speed of sound reduction and fitting of the transport coefficients (kinetic viscosity, thermal conductivity and species diffusion coefficients). It was demonstrated that the above mentioned actions did not lead to relevant changes in the results for the range of considered conditions. On the other hand, the results are in general dependent on the chemical mechanism and care must be taken to use a mechanism that represents well the examined situation.

A sensitivity analysis was performed that showed that the solid conversion rate can be affected by different parameters (diffusion coefficients, surface kinetics and gas phase kinetics). Which of these parameters is the most important, depends on whether the conversion is controlled by the reaction kinetics or the reactant diffusion. For most of the studied particle surface temperatures, the conversion was found to be controlled by the oxygen diffusion to the particle (around $1400 < T_p < 1800$ K) and to the effective flame ($T_p > 1800$ K) surfaces. Even though in diffusion-controlled conditions the overall solid conversion rate is only weakly dependent on kinetics, the contributions from gasification and oxidation reactions, as well as the flame structure, might be substantially affected.

It is remarkable that the combustion behavior of the solid particle can be explored in such a detailed manner by employing a very simple chemical mechanism. However, a complex mechanism is needed for a more thorough analysis. At the current stage of development, the model presented in this study was validated against quasi-steady experimental results. In order to explore transient phenomena in further studies, it would be necessary to account for the heat transfer at the particle surface, in particular radiation between the particle and the surrounding gas, and for temperature gradients inside the particle. Finally, the reason for the conversion rate to drop around $T_p = 1700$ K could be explored by including models that account for changes in the molecular structure of the solid.

Declaration of Competing Interest

The authors declare that they have no known competing financial interests or personal relationships that could have appeared to influence the work reported in this paper.

Acknowledgments

This study has been supported by the statutory research fund of the Silesian University of Technology, Faculty of Energy and Environmental Engineering, Department of Thermal Engineering, Gliwice, Poland. The research leading to these results has also received funding from the research projects: 'CHEERS', financed by the European Union's Horizon 2020 research and innovation program (grant agreement No. 764697).

Appendix A. Derivation of boundary conditions for species

Species transport equation,

$$\frac{\partial(\rho Y_k)}{\partial t} + \nabla \cdot (\rho \mathrm{u} Y_k + \mathbb{J}_k) = \dot{\omega}_k, \tag{A.1}$$

can be expressed in integral form as

$$\int_V \frac{\partial(\rho Y_k)}{\partial t} dV + \int_V \nabla \cdot (\rho \mathrm{u} Y_k + \mathbb{J}_k) dV = \int_V \dot{\omega}_k dV. \tag{A.2}$$

Using the divergence theorem, Eq. (A.2) becomes

$$\int_V \frac{\partial(\rho Y_k)}{\partial t} dV + \int_S (\rho \mathrm{u} Y_k + \mathbb{J}_k) \cdot \hat{\boldsymbol{n}} dA = \int_V \dot{\omega}_k dV, \tag{A.3}$$

where $\hat{\boldsymbol{n}}$ is a unit vector normal to the surface. At the particle surface all volumetric integrals tend to 0 and a source term due to the surface reactions ($\dot{m}_k$) appears in the place of the volumetric reaction term ($\dot{\omega}_k$). Also, since the particle is assumed to be perfectly cylindrical $\hat{\boldsymbol{n}} = \hat{\boldsymbol{r}}$, where $\hat{r}$ is a unit normal vector in the radial direction. After taking all of the above into account, Eq. (A.3) becomes

$$\int_S (\rho \mathrm{u} Y_k + \mathbb{J}_k) \cdot \hat{\boldsymbol{r}} dA = \int_S \dot{m}_k dA. \tag{A.4}$$

Using the fact that for an arbitrary surface

$$\int_S b dA = \int_S c dA \Leftrightarrow b = c, \tag{A.5}$$

Eq. (A.4) can be written in a differential form

$$(\rho \mathrm{u} Y_k + \mathbb{J}_k) \cdot \hat{\boldsymbol{r}} = \dot{m}_k. \tag{A.6}$$

Summing over all gas phase species one obtains

$$\sum_k (\rho \mathrm{u} Y_k + \mathbb{J}_k) \cdot \hat{\boldsymbol{r}} = \rho u_r = \sum_k \dot{m}_k = -\dot{m}_C \tag{A.7}$$

where it has been used that $\sum_k \mathbb{J}_k \cdot \hat{\boldsymbol{r}} = 0$. Here, $\dot{m}_C$ is a carbon consumption rate and u_r is the outward velocity of the species mixture in the radial direction. One can now substitute

$$\mathbb{J}_k = -\rho D_k \nabla Y_k, \tag{A.8}$$

$$\mathrm{u} \cdot \hat{\boldsymbol{r}} = u_r = -\dot{m}_C / \rho \tag{A.9}$$

and

$$\nabla Y_k \cdot \hat{\boldsymbol{r}} = \frac{\partial Y_k}{\partial r} \tag{A.10}$$

into Eq. (A.6) to arrive at the final form of boundary conditions for species mass fractions at the particle surface,

$$\dot{m}_k + \dot{m}_C Y_k + \rho D_k \frac{\partial Y_k}{\partial r} = 0. \tag{A.11}$$

References

[1] Coal 2018Technical Report, International Energy Agency, Paris, 2020. www.iea.org/reports/coal-2020

[2] Renewables 2020Technical Report, International Energy Agency, Paris, 2020. https://www.iea.org/reports/renewables-2020

[3] World Energy Outlook 2020Technical Report, International Energy Agency, Paris, 2020. https://www.iea.org/reports/world-energy-outlook-2020

[4] T. Hara, M. Muto, T. Kitano, R. Kurose, S. Komori, Direct numerical simulation of a pulverized coal jet flame employing a global volatile matter reaction scheme based on detailed reaction mechanism, Combust. Flame 162 (12) (2015) 4391–4407, doi:10.1016/J.COMBUSTFLAME.2015.07.027.

[5] K. Luo, Y. Bai, T. Jin, K. Qiu, J. Fan, Direct numerical simulation study on the stabilization mechanism of a turbulent lifted pulverized coal jet flame in a heated coflow, Energy Fuels 31 (8) (2017) 8742–8757, doi:10.1021/acs.energyfuels.7b01342.

[6] K. Luo, C. Mao, J. Fan, Z. Zhuang, N. Haugen, Fully resolved simulations of single char particle combustion using a ghost-cell immersed boundary method, AIChE J. 64 (7) (2018) 2851–2863, doi:10.1002/aic.16136.

[7] M. Muto, K. Yuasa, R. Kurose, Numerical simulation of ignition in pulverized coal combustion with detailed chemical reaction mechanism, Fuel 190 (2017) 136–144, doi:10.1016/j.fuel.2016.11.029.

[8] M. Rieth, A. Kempf, A. Kronenburg, O. Stein, Carrier-phase DNS of pulverized coal particle ignition and volatile burning in a turbulent mixing layer, Fuel 212 (2018) 364–374, doi:10.1016/J.FUEL.2017.09.096.

[9] X. Wen, A. Shamooni, O.T. Stein, L. Cai, A. Kronenburg, H. Pitsch, A.M. Kempf, C. Hasse, Detailed analysis of early-stage NOxformation in turbulent pulverized coal combustion with fuel-bound nitrogen, Proc. Combust. Inst. volume 38 (2021) 4111–4119, doi:10.1016/j.proci.2020.06.317. Elsevier

[10] J.G.M Kuerten, Point-particle DNS and LES of particle-Laden turbulent flow - a state-of-the-art review, Flow Turbul. Combust. 97 (3) (2016) 689–713, doi:10.1007/s10494-016-9765-y.

[11] M. Vascellari, H. Xu, C. Hasse, Flamelet modeling of coal particle ignition, Proc. Combust. Inst. 34 (2) (2013) 2445–2452, doi:10.1016/j.proci.2012.06.152.

[12] G.L. Tufano, O.T. Stein, A. Kronenburg, A. Frassoldati, T. Faravelli, L. Deng, A.M. Kempf, M. Vascellari, C. Hasse, Resolved flow simulation of pulverized coal particle devolatilization and ignition in air- and O_2/CO_2-atmospheres, Fuel 186 (2016) 285–292, doi:10.1016/j.fuel.2016.08.073.

[13] G.L. Tufano, O.T. Stein, B. Wang, A. Kronenburg, M. Rieth, A.M. Kempf, Coal particle volatile combustion and flame interaction. Part I: characterization of transient and group effects, Fuel 229 (2018) 262–269, doi:10.1016/j.fuel.2018.02.105.

[14] G.L. Tufano, O.T. Stein, B. Wang, A. Kronenburg, M. Rieth, A.M. Kempf, Coal particle volatile combustion and flame interaction. Part II: effects of particle Reynolds number and turbulence, Fuel 234 (2018) 723–731, doi:10.1016/j.fuel.2018.07.054.

[15] M. Kestel, P. Nikrityuk, O. Hennig, C. Hasse, Numerical study of the partial oxidation of a coal particle in steam and dry air atmospheres, IMA J. Appl. Math. (Inst. Math. Appl.) volume 77 (2012) 32–46, doi:10.1093/imamat/hxr071. Oxford University Press

[16] A. Richter, P.A. Nikrityuk, M. Kestel, Numerical investigation of a chemically reacting carbon particle moving in a hot O_2/CO_2 atmosphere, Ind. Eng. Chem. Res. 52 (16) (2013) 5815–5824, doi:10.1021/ie302770j.

[17] D. Safronov, M. Kestel, P. Nikrityuk, B. Meyer, Particle resolved simulations of carbon oxidation in a laminar flow, Can. J. Chem. Eng. 92 (10) (2014) 1669–1686, doi:10.1002/cjce.22017.

[18] S. Schulze, P. Nikrityuk, F. Compart, A. Richter, B. Meyer, Particle-resolved numerical study of char conversion processes in packed beds, Fuel 207 (2017) 655–662, doi:10.1016/j.fuel.2017.05.071.

[19] Z. Xue, Q. Guo, Y. Gong, J. Xu, G. Yu, Numerical study of a reacting single coal char particle with different pore structures moving in a hot O_2/CO_2 atmosphere, Fuel 206 (2017) 381–389, doi:10.1016/j.fuel.2017.06.035.

[20] Z. Xue, Y. Gong, Q. Guo, Y. Wang, G. Yu, Conversion characteristics of a single coal char particle with high porosity moving in a hot O_2/CO_2 atmosphere, Fuel 256 (2019) 115967, doi:10.1016/j.fuel.2019.115967.

[21] A. Richter, M. Kestel, P.A. Nikrityuk, Pore-resolved simulation of char particle combustion/gasification, Gasification Processes: Modeling and Simulation, Wiley-VCH (2014), pp. 243–270.

[22] J. Lee, A. Tomboulides, S. Orszag, R. Yetter, F. Dryer, A transient two-dimensional chemically reactive flow model: fuel particle combustion in a nonquiescent environment, Symp. (Int.) Combust. 26 (2) (1996) 3059–3065, doi:10.1016/S0082-0784(96)80149-4.

[23] S. Farazi, M. Sadr, S. Kang, M. Schiemann, N. Vorobiev, V. Scherer, H. Pitsch, Resolved simulations of single char particle combustion in a laminar flow field, Fuel 201 (2017) 15–28, doi:10.1016/j.fuel.2016.11.011.

[24] T. Sayadi, S. Farazi, S. Kang, H. Pitsch, Transient multiple particle simulations of char particle combustion, Fuel 199 (2017) 289–298, doi:10.1016/j.fuel.2017.02.096.

[25] G.L. Tufano, O.T. Stein, A. Kronenburg, G. Gentile, A. Stagni, A. Frassoldati, T. Faravelli, A.M. Kempf, M. Vascellari, C. Hasse, Fully-resolved simulations of coal particle combustion using a detailed multi-step approach for heterogeneous kinetics, Fuel 240 (2019) 75–83, doi:10.1016/j.fuel.2018.11.139.

[26] C.B. Nguyen, J. Scherer, M. Hartwich, A. Richter, The morphology evolution of char particles during conversion processes, Combust. Flame 226 (2021) 117–128, doi:10.1016/j.combustflame.2020.11.038.

[27] A. Brandenburg, A. Johansen, P.A. Bourdin, W. Dobler, W. Lyra, M. Rheinhardt, S. Bingert, N.E.L. Haugen, A. Mee, F. Gent, N. Babkovskaia, C.-C. Yang, T. Heinemann, B. Dintrans, D. Mitra, S. Candelaresi, J. rn Warnecke, P.J. Käpylä, A. Schreiber, P. Chatterjee, M.J. Käpylä, X.-Y. Li, J.K. ger, J. rgen R. Aarnes, G.R. Sarson, J.S. Oishi, J. Schober, R. Plasson, C. Sandin, E. Karchniwy, L.F.S. Rodrigues, A. Hubbard, G. Guerrero, A. Snodin, I.R. Losada, J. Pekkilä, C. Qian, The pencil code, a modular MPI code for partial differential equations and particles: multipurpose and multiuser-maintained, J. Open Source Softw. 6 (58) (2021) 2807, doi:10.21105/joss.02807.

[28] S.E. Sherer, J.N. Scott, High-order compact finite-difference methods on general overset grids, J. Comput. Phys. 210 (2) (2005) 459–496, doi:10.1016/j.jcp.2005.04.017.

[29] J. Chicheportiche, X. Gloerfelt, Study of interpolation methods for high-accuracy computations on overlapping grids, Comput. Fluids 68 (2012) 112–133, doi:10.1016/j.compfluid.2012.07.019.

[30] M.R. Visbal, D.V. Gaitonde, High-order-accurate methods for complex unsteady subsonic flows, AIAA J. 37 (10) (1999) 1231–1239, doi:10.2514/2.591.

[31] M.R. Visbal, D.V. Gaitonde, On the use of higher-order finite-difference schemes on curvilinear and deforming meshes, J. Comput. Phys. 181 (1) (2002) 155–185, doi:10.1006/jcph.2002.7117.

[32] J.R. Aarnes, N.E.L. Haugen, H.I. Andersson, High-order overset grid method for detecting particle impaction on a cylinder in a cross flow, Int. J. Comput. Fluid Dyn. 33 (1–2) (2019) 43–58, doi:10.1080/10618562.2019.1593385.

[33] J.R. Aarnes, T. Jin, C. Mao, N.E.L. Haugen, K. Luo, H.I. Andersson, Treatment of solid objects in the pencil code using an immersed boundary method and overset grids, Geophys. Astrophys. Fluid Dyn. 114 (1–2) (2020) 35–57, doi:10.1080/03091929.2018.1492720.

[34] N. Babkovskaia, N.E. Haugen, A. Brandenburg, A high-order public domain code for direct numerical simulations of turbulent combustion, J. Comput. Phys. 230 (1) (2011) 1–12, doi:10.1016/j.jcp.2010.08.028.

[35] S.R. Turns, An introduction to combustion: concepts and applications, Second Edition., McGraw Hills International Editions, 2000.

[36] L. Zhang, K. Liu, C. You, Fictitious domain method for fully resolved reacting gas-solid flow simulation, J. Comput. Phys. 299 (2015) 215–228, doi:10.1016/j.jcp.2015.07.010.

[37] F.L. Dryer, C.K. Westbrook, Simplified reaction mechanisms for the oxidation of hydrocarbon fuels in flames, Combust. Sci. Technol. 27 (1–2) (1981) 31–43, doi:10.1080/00102208108946970.

[38] N.E.L. Haugen, R.E. Mitchell, M.B. Tilghman, A comprehensive model for char particle conversion in environments containing O_2 and CO_2, Combust. Flame 162 (2015) 1455–1463, doi:10.1016/j.combustflame.2014.11.015.

[39] A. Makino, T. Namikiri, K. Kimura, Combustion rates of graphite rods in the forward stagnation field with high-temperature airflow, Combust. Flame 132 (4) (2003) 743–753, doi:10.1016/S0010-2180(02)00537-0.

[40] S. Gordon, B. Mcbride, Computer program for calculation of complex chemical equilibrium compositions, NASA Reference Publication, 1971. 1311

[41] A. Brandenburg, Computational aspects of astrophysical MHD and turbulence, Advances in Nonlinear Dynamos, CRC Press (2003), pp. 269–344, doi:10.1201/9780203493137-9.

[42] P.A. Nikrityuk, M. Gräbner, M. Kestel, B. Meyer, Numerical study of the influence of heterogeneous kinetics on the carbon consumption by oxidation of a single coal particle, Fuel 114 (2013) 88–98, doi:10.1016/j.fuel.2012.10.037.

[43] R.T. Yang, M. Steinberg, A diffusion cell method for studying heterogeneous kinetics in the chemical reaction/diffusion controlled region. kinetics of c + $CO_2 \rightarrow$ 2CO at 1200–1600 °c, Ind. Eng. Chem. Fundam. 16 (2) (1977) 235–242, doi:10.1021/i160062a011.

[44] D.E. Rosner, H.D. Allendor, Comparative studies of the attack of pyrolytic and isotropic graphite by atomic and molecular oxygen at high temperatures, AIAA J. 6 (4) (1968) 650–654, doi:10.2514/3.4558.

[45] D.E. Rosner, High-temperature gas-solid reactions, Annu. Rev. Mater. Sci. 2 (1) (1972) 573–606, doi:10.1146/annurev.ms.02.080172.003041.

[46] J. Nagle, R.F. Strickland-Constable, Oxidation of carbon between 1000–2000 °C, Fifth Conference on Carbon, Pergamon (1962), pp. 154–164, doi:10.1016/B978-0-08-009707-7.50026-1.

[47] J.R. Walls, R.F. Strickland-Constable, Oxidation of carbon between 1000-2400 °C, Carbon 1 (3) (1964) 333–338, doi:10.1016/0008-6223(64)90288-x.

[48] A. Makino, N. Araki, Y. Mihara, Combustion of artificial graphite in stagnation flow: Estimation of global kinetic parameters from experimental results, Combust. Flame 96 (3) (1994) 261–274, doi:10.1016/0010-2180(94)90013-2.

[49] A. Makino, T. Namikiri, N. Araki, Combustion rate of graphite in a high stagnation flowfield and its expression as a function of the transfer number, Symp. (Int.) Combust. volume 27 (1998) 2949–2956, doi:10.1016/S0082-0784(98)80154-9. Elsevier

[50] P.A. Libby, T.R. Blake, Theoretical study of burning carbon particles, Combust. Flame 36 (C) (1979) 139–169, doi:10.1016/0010-2180(79)90056-7.

[51] A. Makino, An approximate explicit expression for the combustion rate of a small carbon particle, Combust. Flame 90 (2) (1992) 143–154, doi:10.1016/0010-2180(92)90116-7.